Andreev spectroscopy of nonhelical spin textures in topological insulators

David J. Alspaugh,[1,*] Mahmoud M. Asmar,[1,2,†] Daniel E. Sheehy [1,‡] and Ilya Vekhter[1,§]

[1]*Department of Physics and Astronomy, Louisiana State University, Baton Rouge, Louisiana 70803-4001, USA*
[2]*Department of Physics, Kennesaw State University, Marietta, Georgia 30060, USA*

We study how nonhelical spin textures affect the proximity-induced superconductivity of topological insulator (TI)-superconductor (SC) interface states. In particular we calculate the conductance of lateral heterojunctions which comprise a TI surface that is only partially covered by a superconducting material. Interface potentials at the TI-SC interface may lead to a Fermi velocity and spin texture mismatch between the two regions of the lateral heterojunction. By enforcing the conservation of current across the interface, we derive the boundary conditions and calculate the conductance in both the normal and superconducting state. The total Andreev conductance is calculated for both *s*-wave and spin-triplet parent SCs, and for several examples of nonhelical spin textures which lead to different Fermi surface mismatches between the two planar regions of the heterojunction. We find that for spin-triplet SCs, nonzero conductance signatures only appear for certain combinations of nonhelical spin textures and parent superconducting material.

I. INTRODUCTION

Topological insulators (TIs) are a class of materials which admit linearly dispersing surface states and preserve time reversal (TR) symmetry [1,2]. At pristine vacuum terminations these surface states have isotropic dispersions and are perfectly helical, such that the spin of the propagating state is perpendicular to the direction of its momentum and is confined within the plane of the termination. The common assumption is that at interfaces of TIs with other materials, the interface states of the TI exhibit these same properties. However, the properties of the interfacial boundary may be qualitatively different than that of a vacuum terminated surface, and the available set of symmetries which the interface states must obey is lower than that of the bulk TI material. Effects from charge redistribution, dangling bonds, and lattice mismatch can introduce TR-preserving interface potentials which lower the symmetry and consequently alter the spin structure and dispersion of the interface states. These states have been shown to exhibit elliptical energy contours and nonhelical spin-momentum locking [3–6].

Some of the most exciting potential applications of TIs focus on the possibility that they may be useful as platforms for performing fault-tolerant quantum computations. For instance, If these materials are placed in contact with superconductors (SCs), the interface state of the TI experiences superconductivity due to the proximity effect. When vortices are present or when placed alongside ferromagnetic systems, these junctions are predicted to host Majorana zero modes [7]. These objects are non-Abelian anyons which have the ability to encode quantum information as they are braided around one another in space [7–9]. However, the realization of Majorana zero modes in experiment has proved elusive [10,11]. These difficulties emphasize the need for a detailed understanding of the physics of topological interfaces. In the case of TI-SC heterostructures, the properties of the induced superconductivity strongly depend on the spin structure of the interface state as well as the properties of the parent SC. Existing conclusions about the interface superconductivity, including the prediction that some parent spin-triplet SCs do not induce superconductivity at the interface at all, have been reached assuming helical TI surface states. In Ref. [4], it was demonstrated that nonhelical spin textures are required in order to observe proximity-induced superconductivity for several classes of parent SCs.

To study the consequences of junctions on the TI interface state, in this work we analyze the conductance signatures of lateral heterojunctions of TI-vacuum and TI-SC interfaces. As shown schematically in Fig. 1, such lateral heterojunctions can be constructed by covering only part of a TI surface with a parent SC, where here we denote the TI-vacuum interface on the $x < 0$ half space as region I and the TI-SC interface on the $x > 0$ half space as region II. While the TI-vacuum interface has perfectly helical surface states, interface potentials between the TI and SC materials result in nonhelical interface states. These new states with their altered spin textures have different anisotropic Fermi velocities compared to the helical states, making the analysis of their junctions nontrivial. In Sec. II we introduce the model for the lateral heterojunction, and by enforcing the conservation of current across the interface between regions I and II in Fig. 1, we develop a formalism allowing us to calculate the normal state

————————
*Present address: Department of Physics and Astronomy, California State University, Northridge, CA 91330; david.alspaugh@csun.edu
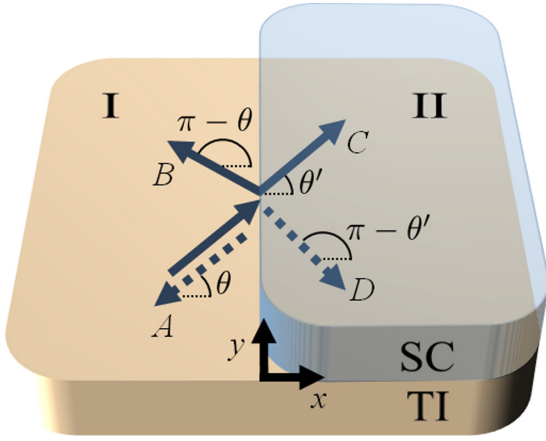†masmar@kennesaw.edu
‡sheehy@lsu.edu
§vekhter@lsu.edu

FIG. 1. Schematic of the superconducting lateral heterojunction. Half of a TI surface is in contact with a superconducting material. Region I on the $x < 0$ half-space defines the TI-vacuum surface, and region II on the $x > 0$ half-space defines the TI-SC interface. Arrows indicate the possible scattering events of normal and Andreev reflection, which determine the conductance of the device. For an electron incoming at angle θ towards the $x = 0$ boundary, these possibilities include Andreev reflection as a hole (A), specular reflection (B), transmission as an electronlike quasiparticle (C), and transmission as a holelike quasiparticle (D).

conductance across the structure. In Sec. III we introduce superconductivity by placing an s-wave SC in region II and calculate the superconducting Andreev conductance across the lateral heterojunction. In Sec. IV we analyze these results for several different experimental setups. We compare how the scattering across the heterojunction described by our formalism compares to the effects of a mismatch in the chemical potential between regions I and II, and we analyze the Andreev conductance arising from several different nonhelical spin textures within region II. In Sec. V we modify our model from Sec. III by introducing spin-triplet SCs within region II, and we analyze the Andreev conductance for parent spin-triplet SCs from the D_{4h} point group. Critically, we find that for certain types of spin-triplet SCs, nonzero conductance signatures exist only if nonhelical spin textures are present in region II. In Sec. VI we summarize our main results and discuss the key experimental consequences of nonhelical spin textures.

II. MODEL OF THE LATERAL HETEROJUNCTION

We begin with a description of the lateral heterojunction in the normal state. As shown in Fig. 1, this device can be created by covering half of a TI surface with a superconducting material. Here we define the $x < 0$ half-space with the TI-vacuum surface as region I, and the $x > 0$ half-space with the TI-SC interface as region II. While region I will host a helical TI surface state with surface state spins confined to the surface (i.e., in the x-y plane of Fig. 1), the material junction in region II can result in interface states with nonhelical spin textures, giving rise to elliptical energy dispersions and spins with components that point out of the plane of the interface (i.e., in the z direction of Fig. 1) [3,4]. To study the heterojunction we therefore write a helical surface Hamiltonian in region I

and include the most general effective linear Hamiltonian that is TR invariant in region II,

$$H = \begin{cases} \hbar v_{\mathrm{F}}(\boldsymbol{\sigma} \times -i\boldsymbol{\nabla})_z - \mu_{\mathrm{L}}, & \text{for } x < 0 \text{ (region I)} \\ \boldsymbol{c} \cdot \boldsymbol{\sigma} - \mu_{\mathrm{R}}, & \text{for } x > 0 \text{ (region II)} \end{cases}. \quad (1)$$

Here $\boldsymbol{\sigma} = (\sigma_x, \sigma_y, \sigma_z)^T$ is a vector of Pauli matrices in spin space, v_{F} is the Fermi velocity, μ_{L} and μ_{R} are the chemical potentials in regions I and II, respectively, and $\boldsymbol{c}$ is a three-component vector defined by $c_i = -i \sum_{j=x,y} c_{ij} \partial_j$. We notice that in the case $\boldsymbol{c}_{\mathrm{D}} = -i\hbar v_{\mathrm{F}}(\partial_y, -\partial_x, 0)^T$ and $\mu_{\mathrm{R}} = \mu_{\mathrm{L}}$, the Hamiltonians of regions I and II are identical and we recover a single TI surface over all space. The presence of nonhelical spin textures in the TI-SC interface of region II can then be encoded in the choice of c_{ij} coefficients [3]. This prescription is valid so long as the transmission between the TI and SC materials is low, so that the TI interface state is still well defined [12,13]. We also note that from the construction of the vector $\boldsymbol{c}$, the form of the Hamiltonian in region II is identical to that of antisymmetric spin-orbit coupling in noncentrosymmetric metals, whose consequences on superconductivity have been extensively studied [14,15]. What is different however is that the usual quadratic energy term is absent, placing us in a regime of infinite spin-orbit coupling strength [16].

A. Examples of nonhelical spin textures

To understand the consequences of nonhelical spin textures as encoded in the vector $\boldsymbol{c}$, it is instructive to first analyze the dispersion relations and spin textures of some specific examples in a spatially homogeneous system. In this case, let us analyze a single TI interface state described by the Hamiltonian

$$H = \boldsymbol{c}(\boldsymbol{k}) \cdot \boldsymbol{\sigma} - \mu. \quad (2)$$

For such a state, both k_x and k_y are good quantum numbers. We introduce $\boldsymbol{c}(\boldsymbol{k})$ as a three-component vector defined by $c_i(\boldsymbol{k}) = \sum_{j=x,y} c_{ij} k_j$. The coefficients c_{ij} must be real for the Hamiltonian to be TR invariant. As discussed in the previous section, a helical TI surface state has the well-known form

$$\boldsymbol{c}_{\mathrm{D}}(\boldsymbol{k}) = \hbar v_{\mathrm{F}}(k_y, -k_x, 0)^T. \quad (3)$$

In this case the dispersion is well understood to have the linear form $\xi(\boldsymbol{k}) = \hbar v_{\mathrm{F}} k - \mu$, admitting a circular Fermi surface and a helical spin texture in which the spin is always perpendicular to the momentum and is confined within the x-y plane. For instance, if the momentum of a surface electron is purely along the x direction, then the spin expectation value is along the negative y direction. The size of the Fermi surface can be changed both by modifying the Fermi velocity v_{F} or by altering the chemical potential μ.

Nonhelical spin textures can result from rotational-symmetry breaking interface potentials within TI and topologically trivial heterostructures, and can introduce elliptical constant energy contours in momentum space and out-of-plane spin textures within the TI interface states [3,4]. Note that these distortions happen even for the lateral heterojunction described in Fig. 1. Two generic examples of such nonhelical spin textures that have been derived from an analysis of the bulk three-dimensional crystal Hamiltonian of a TI interface with a TR-symmetry preserving interface potential

(a) $\quad c(k) = c_D(k)$
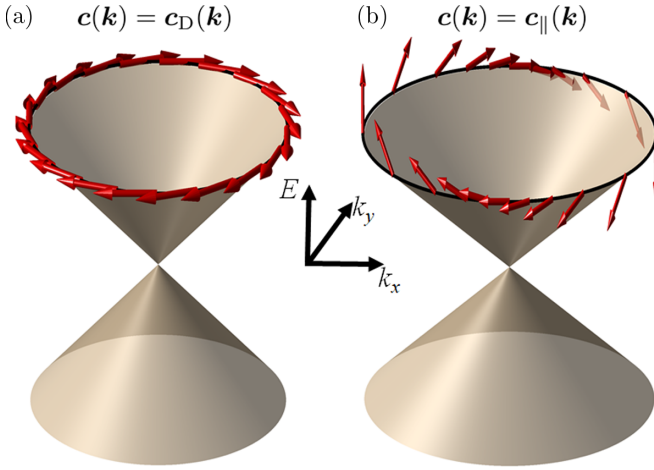
(b) $\quad c(k) = c_\parallel(k)$

FIG. 2. Comparison of the dispersion relations and spin textures of helical and nonhelical TI interface states. (a) Helical system with a surface Hamiltonian defined by $c(k) = c_D(k)$ as expressed in Eq. (3). (b) Nonhelical system with an interface Hamiltonian defined by $c(k) = c_\parallel(k)$ as expressed in Eq. (4). In this example, the TI interface state possesses an out-of-plane spin component that is maximized along the $\pm k_x$ momentum directions.

in the $z = 0$ plane can be modeled by

$$
\begin{aligned}
c_\perp(k) &= \hbar v_F(\lambda k_y, -k_x, -\lambda k_y)^T, \\
c_\parallel(k) &= \hbar v_F(k_y, -\lambda k_x, -\lambda k_x)^T,
\end{aligned} \quad (4)
$$

where $0 < \lambda < 1$ [4]. The former spin texture introduces an elliptical Fermi surface with a major axis perpendicular to the x axis, while the latter spin texture has an elliptical Fermi surface with a major axis parallel to the x axis. In Fig. 2 we compare the dispersions and spin textures of the helical system given by $c_D(k)$ to those of the nonhelical system given by $c_\parallel(k)$. In addition to the ellipticity of the Fermi surface, we can see that if the momentum of an interface electron is purely along x, then the spin expectation value has a nonzero out-of-plane component along the negative z direction. Here we also emphasize that even though these states are nonhelical, the systems described by $c_\perp(k)$ and $c_\parallel(k)$ still fully preserve TR symmetry. Indeed, as pointed out above, the Hamiltonian of Eq. (2) is TR invariant so long as each of the c_{ij} coefficients are real valued. The nonhelical nature of these states is manifested in the winding of their spins about an axis that is not normal to the plane of the interface [3].

B. Boundary conditions

To calculate the normal state conductance of the lateral heterojunction described by Eq. (1), we must solve the scattering problem in which incoming electrons in region I of Fig. 1 may either specularly reflect at the $x = 0$ boundary or transmit into region II. Matching the wave functions at the boundary is nontrivial, however, as the Hamiltonians of the two regions have different Fermi velocities. We proceed to match the wave functions in a way that conserves the total current across the interface of regions I and II.

The effective long-wavelength description cannot account for the rapid variations of the wave functions in the vicinity of

the potential edge at $x = 0$. Therefore, due to the fact that we only have a linear Hamiltonian, in this approach the envelope wave function is not continuous [17–20]. Instead it satisfies

$$
\psi_I(0, y) = \mathcal{M} \psi_{II}(0, y), \quad (5)
$$

for some matrix $\mathcal{M}$ and wave functions $\psi_I(r)$ and $\psi_{II}(r)$ in regions I and II, respectively. In order for this to be a valid boundary value relation for our system, and hence valid for all wave functions of the Hilbert space, the boundary conditions of the wave functions in Eq. (5) must ensure that the Hamiltonian of the entire system is Hermitian. That is, if both $\psi_1(r)$ and $\psi_2(r)$ are wave functions for all x that belong to H, we must have the inner product relations $\langle \psi_1 | H \psi_2 \rangle = \langle H \psi_1 | \psi_2 \rangle$. Inserting Eq. (5) into this condition for hermiticity and integrating by parts, we find

$$
-\hbar v_F \mathcal{M}^\dagger \sigma_y \mathcal{M} = \sum_{i=x,y,z} c_{ix} \sigma_i. \quad (6)
$$

Since the current operator is $j_i \propto \partial H / \partial k_i$, the condition expressed in Eq. (6) is identical to that obtained by conserving the x component of the current across the $x = 0$ interface [21]. To explicitly solve for each element in $\mathcal{M}$, it is helpful to restrict the form of $\mathcal{M}$ by requiring that it must also respect the discrete symmetries of the system. We let $\psi(r)$ be a wave function over all space such that

$$
\psi(r) = \begin{cases} \psi_I(r) & \text{for } x < 0 \\ \psi_{II}(r) & \text{for } x > 0 \end{cases}, \quad (7)
$$

and write $\mathcal{T} = i\sigma_y K$ as the TR symmetry operator where K is complex conjugation. Because the system preserves TR symmetry, we know that $\mathcal{T}\psi(r)$ is also a wave function of our system. Equation (5) holds for all wave functions in the Hilbert space, which implies both $\psi_I(0, y) = \mathcal{M}\psi_{II}(0, y)$ and $\mathcal{T}\psi_I(0, y) = \mathcal{M}\mathcal{T}\psi_{II}(0, y)$. However, by applying $\mathcal{T}$ on the left of both sides of Eq. (5), we have $\mathcal{T}\psi_I(0, y) = \mathcal{T}\mathcal{M}\psi_{II}(0, y)$. This demonstrates that the commutator $[\mathcal{T}, \mathcal{M}] = 0$. This condition implies that $\mathcal{M}$ must take the form $\mathcal{M} = \gamma_0 \sigma_0 + i(\gamma_x \sigma_x + \gamma_y \sigma_y + \gamma_z \sigma_z)$, where all the γ_i are purely real. With this restriction, Eq. (6) can be solved to explicitly find each component of $\mathcal{M}$ such that there is only one remaining free parameter. Simplifying the notation by writing $\gamma_y = \sqrt{v/v_F} \sin \beta$, where $v = (\sqrt{\sum_i c_{ix}^2} - c_{yx})/2\hbar$, we obtain

$$
\mathcal{M}(\beta) = \sqrt{\frac{v}{v_F}} \left[e^{i\sigma_y \beta} + \frac{i}{2\hbar v}(c_{xx}\sigma_z - c_{zx}\sigma_x)e^{-i\sigma_y \beta} \right]. \quad (8)
$$

Here β is a free parameter such that $\beta \in [0, 2\pi)$. Expressing γ_y in this way ensures that all of the coefficients γ_i are real-valued.

In the special case that region II has a helical surface state identical to region I [setting $c = c_D$ and $\mu_R = \mu_L$ in Eq. (1)], the parameter β can be understood in physical terms. From Eq. (8), the boundary value matrix has the form $\mathcal{M}(\beta) = e^{i\sigma_y \beta}$, describing a rotation of the spin of the state about the y axis by an angle of 2β. Because the current density operator along the x direction is proportional to σ_y, this rotation leaves the total current along the x direction invariant [21]. Additionally, in this case only, the value of β can be related to the

strength of a Dirac delta barrier located at the $x = 0$ boundary. By analyzing the Hamiltonian $H = \hbar v_F (\boldsymbol{\sigma} \times \boldsymbol{k})_z - \mu + \alpha \delta(x)$, it can similarly be shown that $\psi(0^-) = e^{-i\alpha/\hbar v_F} \psi(0^+)$, demonstrating that $\beta = -\alpha/\hbar v_F$ [22]. In general, the boundary conditions enforced by $\mathcal{M}(\beta)$ in Eq. (8) similarly reflect the boundary potentials and guarantee the self-adjointness of the total Hamiltonian in Eq. (1) [17,19,21–31].

C. Normal state conductance

Now that we can match the wave functions at the $x = 0$ boundary between regions I and II, the next step is to solve the scattering problem to obtain the normal state conductance of the lateral heterojunction. We consider an incoming electron in region I of Fig. 1 with momentum $\boldsymbol{k}_1 = (k_x, k_y)^T$ and in-plane momentum angle $\theta = \tan^{-1} k_y/k_x$, a specularly reflected electron with momentum $\boldsymbol{k}_2 = (-k_x, k_y)^T$, and a transmitted electron in region II with momentum $\boldsymbol{k}_1' = (k_x', k_y)^T$. The outgoing angle θ' may be solved for in terms of the incoming angle due to the conservation of normal state energy and the conservation of the k_y momentum. The wave function in region I is given by

$$\psi_I(\boldsymbol{r}) = \frac{e^{i\boldsymbol{k}_1 \cdot \boldsymbol{r}}}{\sqrt{2}} \begin{pmatrix} 1 \\ -ie^{i\theta} \end{pmatrix} + r \frac{e^{i\boldsymbol{k}_2 \cdot \boldsymbol{r}}}{\sqrt{2}} \begin{pmatrix} 1 \\ ie^{-i\theta} \end{pmatrix}. \quad (9)$$

In region II the wave function is

$$\psi_{II}(\boldsymbol{r}) = t e^{i\boldsymbol{k}_1' \cdot \boldsymbol{r}} \begin{pmatrix} \cos(\vartheta_{\boldsymbol{c}(\boldsymbol{k}_1')}/2) \\ e^{i\varphi_{\boldsymbol{c}(\boldsymbol{k}_1')}} \sin(\vartheta_{\boldsymbol{c}(\boldsymbol{k}_1')}/2) \end{pmatrix}. \quad (10)$$

Here $\vartheta_{\boldsymbol{c}(\boldsymbol{k}_1')}$, $\varphi_{\boldsymbol{c}(\boldsymbol{k}_1')}$ are the polar and azimuthal angles of the vector $\boldsymbol{c}(\boldsymbol{k}_1')$, respectively, where $\boldsymbol{c}(\boldsymbol{k})$ is defined by $c_i(\boldsymbol{k}) = \sum_{j=x,y} c_{ij} k_j$, and r and t are the coefficients for the reflected and transmitted parts of the wave function, respectively. Matching the wave functions at the $x = 0$ boundary by using Eq. (5), we solve for the reflection coefficient r and define the normal state conductance as

$$\sigma_N(\theta, \beta) = 1 - |r(\theta, \beta)|^2. \quad (11)$$

To demonstrate the consequences of the free parameter β on the normal state conductance, we analyze σ_N in the case when both regions I and II are described by helical Hamiltonians and set $\boldsymbol{c} = \boldsymbol{c}_D$ in Eq. (1). When β is zero, the conductance is always unity (in this case the heterojunction of Fig. 1 is equivalent to one single region of a TI surface). However, when β is nonzero the conductance decreases for nonzero angles. As shown in Fig. 3, the most dramatic changes occur for $\beta = \pi/2$. We see that β acts as an angle-dependent scattering amplitude localized at $x = 0$ between the two planar regions. Incoming electrons with $\theta = 0$ experience full transmission into region II as Dirac particles are incapable of back-scattering from normal incidence due to Klein tunneling [32–35]. This feature of Dirac particles is generally true for TR invariant systems as counter-propagating modes form Kramers' pairs.

III. SUPERCONDUCTING LATERAL HETEROJUNCTIONS

Having discussed the normal state of the lateral heterojunction, we now analyze the superconducting state. To calculate the conductance of the device shown in Fig. 1, we first focus
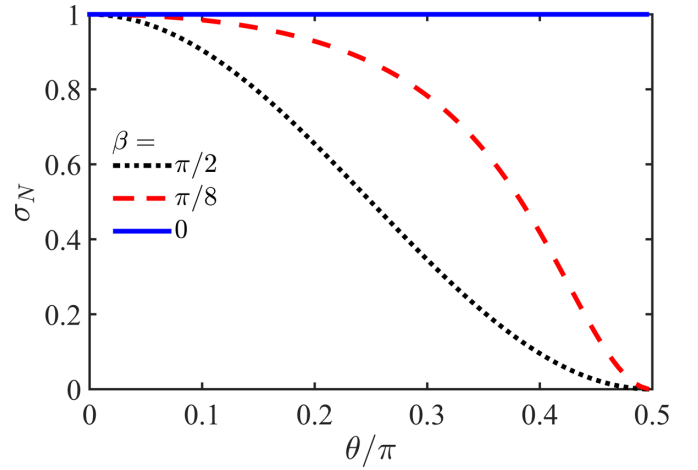

FIG. 3. Normal state conductance $\sigma_N(\theta, \beta)$ as given by Eq. (11) for a lateral heterojunction between two helical surface Hamiltonians with the same Fermi velocity. We see that β acts as an angle-dependent scattering amplitude at the one dimensional interface between regions I and II of the lateral heterojunction.

on region II and derive the proximity-induced superconducting order parameter of the TI-SC interface. We then use the Andreev equations to solve for the wave functions and find the conductance of the normal-superconducting junction of regions I and II [36–39]. To obtain the conductance we solve the Andreev reflection scattering problem in which an incoming electron from region I may either be specularly reflected at the $x = 0$ boundary, or be retroreflected as a hole, corresponding to scattering events B and A in Fig. 1, respectively. Once again matching the wave functions is nontrivial, and we employ the boundary conditions derived above in the form suitable to treat superconductivity.

Focusing on region II, we can obtain the form of the proximity-induced order parameter of the TI-SC interface by projecting the Cooper pair structure of the parent SC onto the eigenstates of the interface Hamiltonian. Writing $(b_{\boldsymbol{k}\uparrow}, b_{\boldsymbol{k}\downarrow})$ as the electron annihilation operators and introducing the Nambu-spinor $\Psi = (b_{\boldsymbol{k}\uparrow}, b_{\boldsymbol{k}\downarrow}, b_{-\boldsymbol{k}\uparrow}^\dagger, b_{-\boldsymbol{k}\downarrow}^\dagger)^T$, the Bogoliubov–de Gennes (BdG) Hamiltonian of the interface may be written as

$$\mathcal{H} = \frac{1}{2} \sum_{\boldsymbol{k}} \Psi^\dagger \begin{pmatrix} H(\boldsymbol{k}) & \hat{\Delta} \\ \hat{\Delta}^\dagger & -H^T(-\boldsymbol{k}) \end{pmatrix} \Psi. \quad (12)$$

Here $H(\boldsymbol{k}) = \boldsymbol{c}(\boldsymbol{k}) \cdot \boldsymbol{\sigma} - \mu_R$ is the interface Hamiltonian in the normal state, and the proximity-induced order parameter is given by $\hat{\Delta} = [\psi(\boldsymbol{k}) + \boldsymbol{d}(\boldsymbol{k}) \cdot \boldsymbol{\sigma}](i\sigma_y)$. The spin-singlet and spin-triplet components of the proximity-induced order are described by $\psi(\boldsymbol{k})$ and $\boldsymbol{d}(\boldsymbol{k})$, respectively. In this section, we focus on the case that the parent material of the heterostructure is an s-wave SC by setting $\psi(\boldsymbol{k}) = \Delta_0$ and $\boldsymbol{d}(\boldsymbol{k}) = 0$. We also note that if the system is driven out of equilibrium, the situation is more complex, and spin-triplet superconductivity can appear even in the absence of magnetic ordering [40].

We then take the weak coupling limit to obtain the BdG wave functions [4]. In the weak coupling limit where $\mu_R \gg \Delta_0$ interband pairing can be ignored. Writing $a_{\boldsymbol{k}} = \cos(\vartheta_{\boldsymbol{c}(\boldsymbol{k})}/2) b_{\boldsymbol{k}\uparrow} + e^{-i\varphi_{\boldsymbol{c}(\boldsymbol{k})}} \sin(\vartheta_{\boldsymbol{c}(\boldsymbol{k})}/2) b_{\boldsymbol{k}\downarrow}$ as the annihilation

operator of the conduction band eigenstate of $H(\boldsymbol{k})$, we find

$$\mathcal{H} \approx \frac{1}{2} \sum_{\boldsymbol{k}} \Phi^{\dagger} \begin{pmatrix} \xi(\boldsymbol{k}) & \Delta(\boldsymbol{k}) \\ \Delta^*(\boldsymbol{k}) & -\xi(\boldsymbol{k}) \end{pmatrix} \Phi. \qquad (13)$$

Here $\Phi = (a_{\boldsymbol{k}}, a_{-\boldsymbol{k}}^{\dagger})^T$ and $\Delta(\boldsymbol{k}) = -e^{-i\varphi_{c(\boldsymbol{k})}}\Delta_0$, with $\vartheta_{c(\boldsymbol{k})}$ and $\varphi_{c(\boldsymbol{k})}$ being the polar and azimuthal angles of the vector $\boldsymbol{c}(\boldsymbol{k})$, respectively. We note that in spin space, the BdG Hamiltonian of Eq. (13) remains a 4×4 matrix, as the conduction band annihilation operator $a_{\boldsymbol{k}}$ is a two-component spinor. The normal state energy is given as $\xi(\boldsymbol{k}) = |\boldsymbol{c}(\boldsymbol{k})| - \mu_{\mathrm{R}}$. In the basis of Eq. (13), the eigenfunction of $\mathcal{H}$ has the form $\phi(\boldsymbol{r}) = (u(\boldsymbol{r}), v(\boldsymbol{r}))^T$.

We may then invoke the Andreev approximation to model the boundary between regions I and II. For a spatially inhomogeneous order parameter, the BdG equations are given by [38]

$$Eu(\boldsymbol{r}_1) = \xi u(\boldsymbol{r}_1) + \int d\boldsymbol{r}_2 \Delta(\boldsymbol{r}_1, \boldsymbol{r}_2) v(\boldsymbol{r}_2),$$
$$\qquad \qquad (14)$$
$$Ev(\boldsymbol{r}_1) = -\xi v(\boldsymbol{r}_1) + \int d\boldsymbol{r}_2 \Delta^*(\boldsymbol{r}_1, \boldsymbol{r}_2) u(\boldsymbol{r}_2).$$

Here $\Delta(\boldsymbol{r}_1, \boldsymbol{r}_2)$ is the two-point correlation function. In the Andreev approximation, we write $\phi(\boldsymbol{r}) = e^{i\boldsymbol{k}_{\mathrm{F}} \cdot \boldsymbol{r}}[U(\boldsymbol{r}), V(\boldsymbol{r})]^T$, where $\boldsymbol{k}_{\mathrm{F}}$ lies on the Fermi surface. By writing $\boldsymbol{R} = (\boldsymbol{r}_1 + \boldsymbol{r}_2)/2$ and $\boldsymbol{s} = \boldsymbol{r}_2 - \boldsymbol{r}_1$ as the center of mass and relative coordinates, respectively, defining $\Delta(\boldsymbol{R}, \boldsymbol{k}) = \int \Delta(\boldsymbol{R}, \boldsymbol{s}) e^{i\boldsymbol{k} \cdot \boldsymbol{s}} d\boldsymbol{s}$, and writing $\xi(\boldsymbol{k}_{\mathrm{F}} - i\nabla) \approx (\partial\xi/\partial\boldsymbol{k})|_{\boldsymbol{k}_{\mathrm{F}}} \cdot (-i\nabla)$, we obtain the Andreev equations [38]

$$EU(\boldsymbol{r}_1) = -i\boldsymbol{v}_{\mathrm{F}}(\boldsymbol{k}_{\mathrm{F}}) \cdot \nabla U(\boldsymbol{r}_1) + \Delta(\boldsymbol{r}_1, \boldsymbol{k}_{\mathrm{F}})V(\boldsymbol{r}_1),$$
$$EV(\boldsymbol{r}_1) = i\boldsymbol{v}_{\mathrm{F}}(\boldsymbol{k}_{\mathrm{F}}) \cdot \nabla V(\boldsymbol{r}_1) + \Delta^*(\boldsymbol{r}_1, \boldsymbol{k}_{\mathrm{F}})U(\boldsymbol{r}_1). \qquad (15)$$

Here $\boldsymbol{v}_{\mathrm{F}}(\boldsymbol{k}_{\mathrm{F}}) = (\partial\xi/\partial\boldsymbol{k})|_{\boldsymbol{k}_{\mathrm{F}}}$, and $\Delta(\boldsymbol{r}_1, \boldsymbol{k}_{\mathrm{F}}) = -e^{-i\varphi_{c(\boldsymbol{k}_{\mathrm{F}})}}\Delta_0 \Theta(x)$. By solving these equations we can obtain the wave functions for our system.

To solve the Andreev scattering problem, we assume a helical surface Hamiltonian in region I and consider an incoming incident electron with momentum $\boldsymbol{k}_1$ and in-plane angle θ. At the boundary, the electron may be retroreflected as a hole with momentum $\boldsymbol{k}_1$ or specularly reflected as an electron with momentum $\boldsymbol{k}_2$, corresponding to scattering events A and B in Fig. 1, respectively. In the spin-space basis of Eq. (12) and setting $H(\boldsymbol{k}) = \hbar v_{\mathrm{F}}(\boldsymbol{\sigma} \times \boldsymbol{k})_z - \mu_{\mathrm{L}}$, the wave function once again has four components and is given by

$$\psi_{\mathrm{I}}(\boldsymbol{r}) = \frac{e^{i\boldsymbol{k}_1^+ \cdot \boldsymbol{r}}}{\sqrt{2}} \begin{pmatrix} 1 \\ -ie^{i\theta} \\ 0 \\ 0 \end{pmatrix} + A\frac{e^{i\boldsymbol{k}_1^- \cdot \boldsymbol{r}}}{\sqrt{2}} \begin{pmatrix} 0 \\ 0 \\ 1 \\ -ie^{-i\theta} \end{pmatrix}$$
$$+ B\frac{e^{i\boldsymbol{k}_2^+ \cdot \boldsymbol{r}}}{\sqrt{2}} \begin{pmatrix} 1 \\ ie^{-i\theta} \\ 0 \\ 0 \end{pmatrix}. \qquad (16)$$

Note that we choose to use the spin basis of Eq. (12) since the helicity basis of Eq. (13) is momentum dependent. Here $\boldsymbol{k}^{\pm} = (k_x^{\pm}, k_y)^T$, where $k_x^{\pm} = k_x \pm E/v_{Fx}(\boldsymbol{k})$. In region II the incident electron can either be transmitted as an electronlike quasiparticle with momentum $\boldsymbol{k}_1'$ and in-plane angle θ' or a

holelike quasiparticle with momentum $\boldsymbol{k}_2' = (-k_x', k_y)^T$, corresponding to scattering events C and D in Fig. 1, respectively. Here we note that due to the translational invariance along the y direction, the k_y momentum is conserved. The nonhelical wave function in region II is then

$$\psi_{\mathrm{II}}(\boldsymbol{r}) = C\frac{e^{i\boldsymbol{k}_1'^+ \cdot \boldsymbol{r}}}{\sqrt{N_-}} \begin{pmatrix} \cos(\vartheta_{c(\boldsymbol{k}_1')}/2) \\ e^{i\varphi_{c(\boldsymbol{k}_1')}}\sin(\vartheta_{c(\boldsymbol{k}_1')}/2) \\ f_-(\boldsymbol{k}_1')\sin(\vartheta_{c(\boldsymbol{k}_1')}/2) \\ -f_-(\boldsymbol{k}_1')e^{-i\varphi_{c(\boldsymbol{k}_1')}}\cos(\vartheta_{c(\boldsymbol{k}_1')}/2) \end{pmatrix}$$
$$+ D\frac{e^{i\boldsymbol{k}_2'^- \cdot \boldsymbol{r}}}{\sqrt{N_+}} \begin{pmatrix} \cos(\vartheta_{c(\boldsymbol{k}_2')}/2) \\ e^{i\varphi_{c(\boldsymbol{k}_2')}}\sin(\vartheta_{c(\boldsymbol{k}_2')}/2) \\ f_+(\boldsymbol{k}_2')\sin(\vartheta_{c(\boldsymbol{k}_2')}/2) \\ -f_+(\boldsymbol{k}_2')e^{-i\varphi_{c(\boldsymbol{k}_2')}}\cos(\vartheta_{c(\boldsymbol{k}_2')}/2) \end{pmatrix}. \qquad (17)$$

Here $N_{\pm}^{-1/2} = \Delta_0/\sqrt{2E(E \pm \sqrt{E^2 - \Delta_0^2})}$ and $f_{\pm}(\boldsymbol{k}) = (E \pm \sqrt{E^2 - \Delta_0^2})/(-e^{-i\varphi_{c(\boldsymbol{k})}}\Delta_0)$. Once again $\vartheta_{c(\boldsymbol{k})}$ and $\varphi_{c(\boldsymbol{k})}$ are the polar and azimuthal angles of the vector $\boldsymbol{c}(\boldsymbol{k})$, respectively. We have that $\boldsymbol{k}'^{\pm} = (k_x'^{\pm}, k_y)^T$ where $k_x'^{\pm} = k_x' \pm \sqrt{E^2 - \Delta_0^2}/v_{Fx}(\boldsymbol{k}')$. As in the previous section the outgoing angle θ' may be solved for in terms of the incoming angle θ due to the conservation of the k_y momentum and the conservation of the normal state energy, noting that $\xi_L(\boldsymbol{k}) = \hbar v_{\mathrm{F}}|\boldsymbol{k}| - \mu_{\mathrm{L}}$ in region I and $\xi_R(\boldsymbol{k}) = |\boldsymbol{c}(\boldsymbol{k})| - \mu_{\mathrm{R}}$ in region II.

To solve the scattering problem we then must match the wave functions at the $x = 0$ boundary. Once again we can generally write

$$\psi_{\mathrm{I}}(0, y) = \mathcal{M}_S \psi_{\mathrm{II}}(0, y). \qquad (18)$$

In the mean-field BdG description the Hamiltonian $\mathcal{H}$ is written in a redundant formalism where the hole degrees of freedom are constructed from the electron Hamiltonian $H(\boldsymbol{k})$ by writing $-H^T(-\boldsymbol{k})$. Following the methods of Sec. II we find that the boundary value matrix for the hole Hamiltonian $-H^T(-\boldsymbol{k})$ is given by $\mathcal{M}^*(\beta)$. Because $-H^T(-\boldsymbol{k})$ is not independent of $H(\boldsymbol{k})$, we see that if $\mathcal{M}(\beta)$ has a particular value for its free parameter β, then $\mathcal{M}^*(\beta)$ must also have this same value for its free parameter. The boundary value matrix for the BdG wave functions is then

$$\mathcal{M}_S(\beta) = \begin{pmatrix} \mathcal{M}(\beta) & 0 \\ 0 & \mathcal{M}^*(\beta) \end{pmatrix}. \qquad (19)$$

The block diagonal nature of the matrix $\mathcal{M}_S(\beta)$ means that there is no additional particle hole mixing due to the boundary conditions, which is a natural assumption.

Matching the wave functions by writing $\psi_{\mathrm{I}}(0, y) = \mathcal{M}_S(\beta)\psi_{\mathrm{II}}(0, y)$ and solving for the coefficients A and B, we then define the transmission coefficient of the superconducting lateral heterojunction [37,39,41] as $\sigma_S(E, \theta, \beta) = 1 + |A|^2 - |B|^2$. From here, we can define the normalized conductance and the total conductance,
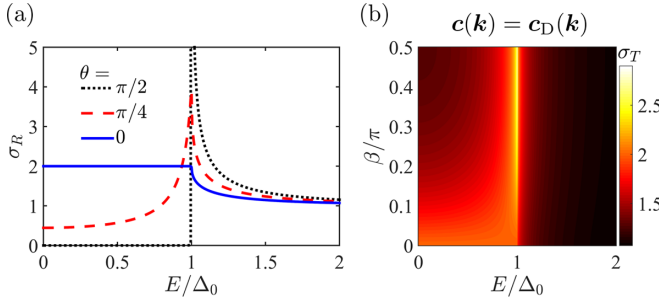
(a)
(b)

FIG. 4. Conductance of the superconducting lateral heterojunction for a parent s-wave SC. (a) Normalized conductance $\sigma_R(E, \theta, \beta)$ for several incident electron angles, such that $c(k) = c_D(k)$ and $\beta = \pi/2$. (b) Total conductance $\sigma_T(E, \beta)$ of the heterojunction such that $c(k) = c_D(k)$. The normalized conductance $\sigma_R(E, \theta, \beta)$ and total conductance $\sigma_T(E, \beta)$ are both defined in Eq. (20).

respectively, as

$$
\sigma_R(E, \theta, \beta) = \frac{\sigma_S(E, \theta, \beta)}{\sigma_N(\theta, \beta)},
$$
$$
\sigma_T(E, \beta) = \frac{\int_{-\pi/2}^{\pi/2} \sigma_S(E, \theta, \beta) \cos\theta \, d\theta}{\int_{-\pi/2}^{\pi/2} \sigma_N(\theta, \beta) \cos\theta \, d\theta}, \tag{20}
$$

where $\sigma_N(\theta, \beta)$ is the normal state conductance given in Eq. (11).

IV. CONDUCTANCE OF THE LATERAL HETEROJUNCTION

In this section we analyze the consequences of nonhelical spin textures, as encoded in the choice of c_{ij} coefficients, on the conductance of superconducting lateral heterostructures with parent s-wave SCs. We first analyze the normalized conductance σ_R in the case that $c(k) = c_D(k)$ in region II, where $c_D(k) = \hbar v_F(k_y, -k_x, 0)^T$ so that both sides of the heterojunction admit helical surface states. We find that when $\beta = 0$ there is no scattering at the junction and all incoming angles experience perfect Andreev reflection for energies below the gap edge. When $\beta = \pi/2$ the probability of specular reflection due to scattering increases, resulting in a suppressed conductance for energies below the gap edge as shown in Fig. 4(a). In the standard treatment by Blonder *et al.*, as the scattering at the junction increases the conductance evolves from the Andreev limit to the profile reflecting the tunneling density of states [37]. Note that this is not what takes place with increasing β: the low energy conductance never vanishes, as seen in the total conductance in Fig. 4(b) and the black dotted line in Fig. 5(a). This is because the normal incidence angle always experience perfect Andreev reflection regardless of the strength of β, reflecting the inability to confine Dirac particles due to Klein tunneling. As in the normal state, Fig. 4(a) shows that β acts as an angle-dependent scattering amplitude. In Fig. 4(b) we plot the total conductance for all $\beta \in [0, \pi/2]$. For $\beta = 0$ we see that we have a constant $\sigma_T(E, 0) = 2$ for all $E < \Delta_0$, followed by a decreasing conductance for larger energies above the superconducting gap. Whenever $\beta \neq 0$ the conductance instead finds a maximum value at the $E = \Delta_0$ gap edge.
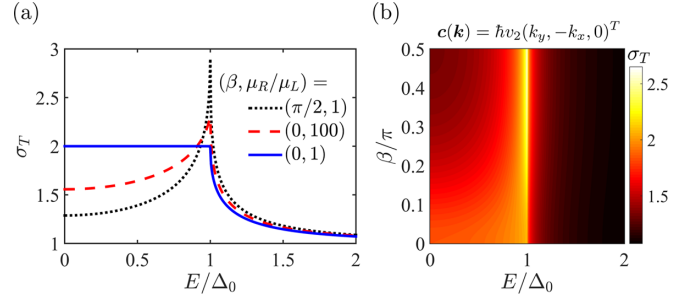
(a)
(b)

FIG. 5. (a) Total conductance $\sigma_T(E, \beta)$ as given by Eq. (20) of the superconducting lateral heterojunction for a parent s-wave SC as $c(k) = c_D(k)$. Here it can be observed that a mismatch in the chemical potentials can introduce a peak at the gap edge, but not as large as the consequences of the angle-dependent scattering amplitude controlled by β localized at the $x = 0$ boundary. (b) Total conductance $\sigma_T(E, \beta)$ of the superconducting lateral heterojunction for a parent s-wave SC in the case that the Fermi velocity in region II is reduced, such that $v_2 = 0.7 v_F$.

For conventional s-wave SCs in a normal-superconducting junction, localized interface potentials at the boundary can result in divergences of the total conductance at the gap edge [37]. This is in contrast to the Dirac Hamiltonians that describe our lateral heterojunction, as the total conductance only obtains a maximum which is largest at the gap edge for $\beta = \pi/2$. The concomitant result is that the total conductance has a maximum, rather than a singularity, at the gap edge.

In Fig. 5(a), we plot the total conductance for the case $c(k) = c_D(k)$ and compare the effects of the angle-dependent scattering controlled by β to that of a mismatch of the chemical potentials between regions I and II. While $\mu_L \neq \mu_R$ similarly creates a maximum at the gap edge, the effect is not as pronounced as that arising from setting $\beta = \pi/2$. In Fig. 5(b) we plot the total conductance in the case that region II has a renormalized Fermi velocity such that $c(k) = \hbar v_2(k_y, -k_x, 0)$, where $v_2 = 0.7 v_F$. The reduced Fermi velocity creates a mismatch in the size of the Fermi surfaces between regions I and II, leading to a reduction in transmission in addition to that controlled by β.

In Figs. 6(a) and 6(b) we plot the total conductance for each of the two nonhelical cases described by Eq. (4). Comparing Figs. 4(b) and 6(b), we see that $c_{\parallel}(k)$ has the same total conductance spectrum as the helical surface states of $c_D(k)$, due to the fact that the conservation of the k_y momentum is unaffected by the ellipticity in this direction. In contrast, the total conductance of $c_{\perp}(k)$ is modified compared to that of the helical surface states. However, for $\beta = \pi/8$ in Fig. 6(a) the scattering of the $x = 0$ boundary is reduced and the system experiences perfect Andreev reflection. It follows that the direction of the ellipticity of the Fermi surface cannot be distinguished from the consequences of β as different choices of β can produce similar conductance spectra between $c_{\perp}(k)$ and $c_{\parallel}(k)$. In addition, we find that different ellipse directions require different values of β to maximize the normal state conductance.
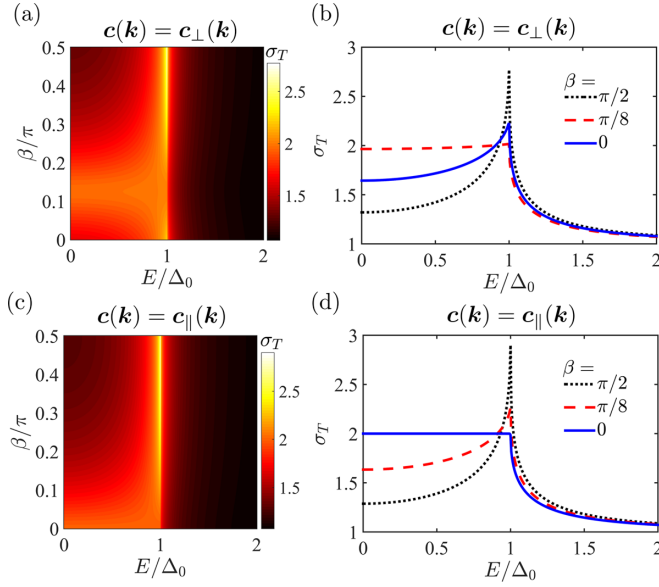
FIG. 6. Total conductance $\sigma_T(E, \beta)$ as given by Eq. (20) of the superconducting lateral heterojunction in the case that region II exhibits nonhelical spin textures. In (a) and (c) we plot the total conductance for the nonhelical spin textures described by $c_\perp(k)$ and $c_\parallel(k)$ as given in Eq. (4), respectively. For both cases we have a parent s-wave SC and $\lambda = 2/3$. In (b) and (d) we plot the same conductance spectra for the indicated values of β.

V. SPIN-TRIPLET SUPERCONDUCTORS

Next we study the conductance signatures for several examples of parent spin-triplet SCs. To analyze these systems, we replace the order parameter of the parent SC in Eq. (12) with $\hat{\Delta} = [d(k) \cdot \sigma](i\sigma_y)$, where the vector $d(k)$ defines the spin-triplet part of the pairing field. Carrying through a similar analysis as before, it has been shown in Ref. [4] that the proximity-induced order parameter of the TI-SC interface in Eq. (13) now takes the form $\Delta(k) = -e^{-i\varphi_{c(k)}}[\hat{c}(k) \cdot d(k)]$, where $\hat{c}(k) = c(k)/|c(k)|$.

For concreteness we assume a tetragonal crystal symmetry for the parent superconducting material and classify $d(k)$ according to the irreducible representations of the D_{4h} point group. The conductance signatures of the chiral $E_{2u}^\pm$ pairing

states in which $d_{E_{2u}^\pm}(k) = \Delta_0(\hat{k}_x \pm i\hat{k}_y)\hat{z}$ have been studied in Ref. [4], and below we focus on the helical A_{1u}, A_{2u}, B_{1u}, and B_{2u} pairing states.

Assuming that $c(k) = c_D(k)$ in region II and thus $\Delta_D(k) = -ie^{-i\theta}[d(k) \times \hat{k}]_z$, we find that the A_{2u} pairing state with $d_{A_{2u}}(k) = \Delta_0(\hat{k}_y\hat{x} - \hat{k}_x\hat{y})$ produces isotropic fully gapped superconductivity at the interface. In contrast, the B_{1u} pairing state with $d_{B_{1u}}(k) = \Delta_0(\hat{k}_x\hat{x} - \hat{k}_y\hat{y})$ and the B_{2u} pairing state with $d_{B_{2u}}(k) = \Delta_0(\hat{k}_y\hat{x} + \hat{k}_x\hat{y})$ both produce d-wave-like nodal gaps. These differences manifest themselves in the Andreev conductance spectra plotted in Fig. 7. For the B_{2u} pairing state at $\beta = 0$ there is a bright spot corresponding to Andreev reflection near $E = 0$. That peak is shifted towards the finite in-gap value as β increases. In contrast, for the B_{1u} pairing state there is a zero energy peak in the total conductance for all values of β. For the A_{1u} pairing state with $d_{A_{1u}}(k) = \Delta_0(\hat{k}_x\hat{x} + \hat{k}_y\hat{y})$ we find that the order parameter vanishes and there is no proximity-induced superconductivity when $c(k) = c_D(k)$. For this family of spin-triplet SCs the proximity effect thus requires the presence of nonhelical spin textures in the TI-SC barrier. In Fig. 8 we plot the total conductance for the nonhelical spin textures described by $c_\perp(k)$ and $c_\parallel(k)$, respectively. In both cases we find that the conductance always obtains its largest value at zero energy regardless of the value of β. As before, the orientation of the elliptical energy contours cannot be distinguished from the effects of scattering as different values of β give rise to similar conductance spectra. We calculate that at energies comparable to the proximity-induced gap edge, the conductance tends towards unity. While we cannot test for the direction of the dispersion's ellipticity, the existence of the anisotropy would be proven by the observation of the signal.

VI. DISCUSSION

In this work we analyzed how nonhelical spin textures present in TI-SC interface states affect the conductance of lateral heterojunctions, which can be created by placing a parent SC in contact with only half of a TI surface as shown schematically in Fig. 1. It has been shown that TI-vacuum terminations host helical surface states such that the total angular momentum of the propagating state is perpendicular to its velocity and confined within the plane of the surface
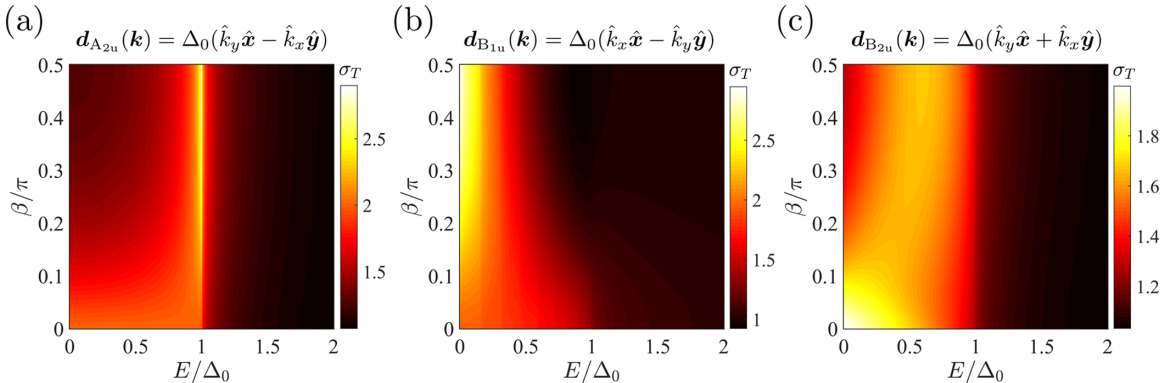

FIG. 7. Total conductance $\sigma_T(E, \beta)$ as given by Eq. (20) for parent helical spin-triplet SCs according to the D_{4h} point group in the case that $c(k) = c_D(k)$ for (a) a parent A_{2u} SC (b) a parent B_{1u} SC (c) a parent B_{2u} SC.
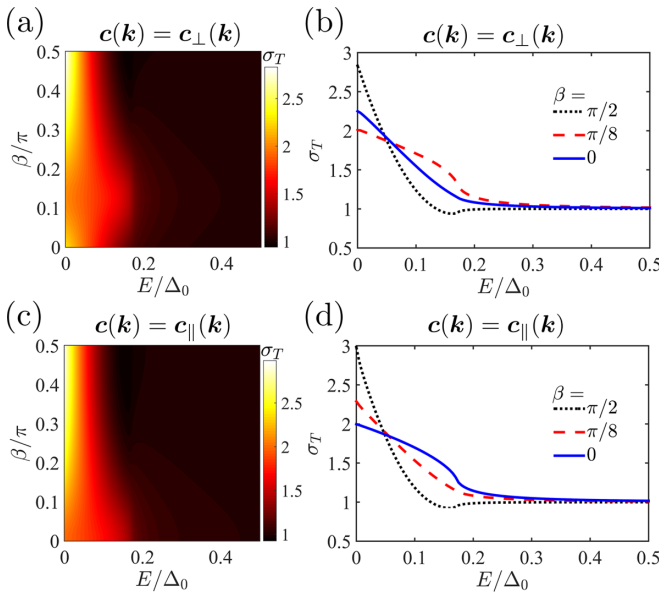
FIG. 8. Total conductance $\sigma_T(E, \beta)$ as given by Eq. (20) for an A_{1u} parent helical spin-triplet SC as defined by the D_{4h} point group. In (a) and (c) we plot the total conductance for the nonhelical spin textures described by $c_\perp(k)$ and $c_\parallel(k)$ as given in Eq. (4) respectively. In (b) and (d) we plot the same conductance spectra for chosen values of β.

[1,2]. In contrast, TIs in contact with nontopological materials host interface states that can exhibit elliptical energy contours and nonhelical spin textures that point out of the plane of the interface [3,4].

We evaluated the conductance of the system in the normal state and found that angle-dependent scattering amplitudes localized at the one-dimensional boundary between the TI-vacuum surface (region I) and the TI-SC interface (region II), as shown schematically in Fig. 1, lead to a reduction of the current through the heterojunction. This reduction is largely due to the scattering of near-grazing angles at the boundary between regions I and II. Introducing s-wave superconductiv-ity, we then found that both the angle-dependent scattering amplitude and a mismatch of the chemical potentials between regions I and II can both reduce the Andreev conductance through the device, with the former leading to a more dramatic suppression. We also calculated the total conductance for a variety of nonhelical spin textures, which all lead to qualitatively similar conductance spectra for parent s-wave SCs characterized by a finite, albeit reduced, conductance at $E = 0$ and a peak at the gap edge. Finally, we then computed the total conductance spectra for parent spin-triplet SCs in region II as classified according to the irreducible representations of the D_{4h} point group. In particular, we find that for parent helical A_{1u} SCs, nonzero conductance spectra only exist when nonhelical spin textures are present within region II.

Our results in general demonstrate that nonhelical spin textures have important and observable consequences for TI-based devices. TI-SC heterostructures placed alongside ferromagnetic materials have earlier been proposed to host Majorana zero modes as a consequence of the spin-momentum locking intrinsic to topological interface states. While the existence of Majorana zero modes within vortex cores depends on the nontrivial spin winding of the interface states around the Fermi surface, which is not directly affected by the nonhelical nature of the states, the associated properties of the quasiparticles are sensitive to the relative orientation of the magnetic field and the axis of the spin winding. We leave this for a future investigation. In this article we show that the spin-momentum locking within heterojunctions is more complex than has been commonly assumed and leads to a more diverse set of phenomena even for nonmagnetic heterostructures. Our work therefore constitutes a crucial step towards understanding the role of nonhelical spin states in such heterostructures.

[1] M. Z. Hasan and C. L. Kane, Rev. Mod. Phys. **82**, 3045 (2010).

[2] X.-L. Qi and S.-C. Zhang, Rev. Mod. Phys. **83**, 1057 (2011).

[3] M. M. Asmar, D. E. Sheehy, and I. Vekhter, Phys. Rev. B **95**, 241115(R) (2017).

[4] D. J. Alspaugh, M. M. Asmar, D. E. Sheehy, and I. Vekhter, Phys. Rev. B **98**, 104516 (2018).

[5] F. Zhang, C. L. Kane, and E. J. Mele, Phys. Rev. B **86**, 081303(R) (2012).

[6] E. Thareja, I. Vekhter, and M. M. Asmar, Phys. Rev. B **102**, 125308 (2020).

[7] L. Fu and C. L. Kane, Phys. Rev. Lett. **100**, 096407 (2008).

[8] N. Read and D. Green, Phys. Rev. B **61**, 10267 (2000).

[9] D. A. Ivanov, Phys. Rev. Lett. **86**, 268 (2001).

[10] H. Zhang, C.-X. Liu, S. Gazibegovic, D. Xu, J. A. Logan, G. Wang, N. van Loo, J. D. S. Bommer, M. W. A. de Moor, D. Car, R. L. M. Op het Veld, P. J. van Veldhoven, S. Koelling, M. A. Verheijen, M. Pendharkar, D. J. Pennachio, B. Shojaei, J. S. Lee, C. J. Palmstrøm, E. P. A. M. Bakkers et al., Nature (London) **556**, 74 (2018).

[11] H. Zhang, C.-X. Liu, S. Gazibegovic, D. Xu, J. A. Logan, G. Wang, N. van Loo, J. D. S. Bommer, M. W. A. de Moor, D. Car, R. L. M. Op het Veld, P. J. van Veldhoven, S. Koelling, M. A. Verheijen, M. Pendharkar, D. J. Pennachio, B. Shojaei, J. S. Lee, C. J. Palmstrøm, E. P. A. M. Bakkers et al., Nature (London) **591**, E30 (2021).

[12] E. Zhao, C. Zhang, and M. Lababidi, Phys. Rev. B **82**, 205331 (2010).

[13] R. Grein, J. Michelsen, and M. Eschrig, J. Phys.: Conf. Ser. **391**, 012149 (2012).

[14] M. Smidman, M. B. Salamon, H. Q. Yuan, and D. F. Agterberg, Rep. Prog. Phys. **80**, 036501 (2017).

[15] K. V. Samokhin, Phys. Rev. B **92**, 174517 (2015).

[16] D. Pesin and A. H. MacDonald, Nat. Mater. **11**, 409 (2012).

[17] M. Tanhayi Ahari, G. Ortiz, and B. Seradjeh, Am. J. Phys. **84**, 858 (2016).

[18] G. Bonneau, J. Faraut, and G. Valent, Am. J. Phys. **69**, 322 (2001).

[19] D. M. Gitman, I. V. Tyutin, and B. L. Voronov, *Self-adjoint Extentions in Quantum Mechanics*, 1st ed., Progress in Mathematical Physics No. 62 (Birkhäuser, Basel, 2012), pp. XIII, 511.

[20] M. Stone and P. Goldbart, *Mathematics for Physics: A Guided Tour for Graduate Students* (Cambridge University Press, Cambridge, 2009).

[21] D. Sen and O. Deb, Phys. Rev. B **85**, 245402 (2012).

[22] B. H. J. McKellar and G. J. Stephenson, Phys. Rev. A **36**, 2566 (1987).

[23] E. McCann and V. I. Fal'ko, J. Phys.: Condens. Matter **16**, 2371 (2004).

[24] A. R. Akhmerov and C. W. J. Beenakker, Phys. Rev. B **77**, 085423 (2008).

[25] C. W. J. Beenakker, Rev. Mod. Phys. **80**, 1337 (2008).

[26] L. Isaev, Y. H. Moon, and G. Ortiz, Phys. Rev. B **84**, 075444 (2011).

[27] L. Isaev, G. Ortiz, and I. Vekhter, Phys. Rev. B **92**, 205423 (2015).

[28] H.-H. Shao, Y.-M. Liu, X.-Y. Zhou, and G.-H. Zhou, Chin. Phys. B **23**, 107304 (2014).

[29] R. Takahashi and S. Murakami, Phys. Rev. Lett. **107**, 166805 (2011).

[30] V. A. Volkov and T. N. Pinsker, Sov. Phys. Solid State **23**, 1022 (1981).

[31] S. Yu. Potapenko and A. M. Satanin, Sov. Phys. Solid State **26**, 1067 (1984).

[32] A. H. Castro Neto, F. Guinea, N. M. R. Peres, K. S. Novoselov, and A. K. Geim, Rev. Mod. Phys. **81**, 109 (2009).

[33] M. I. Katsnelson, K. S. Novoselov, and A. K. Geim, Nat. Phys. **2**, 620 (2006).

[34] P. E. Allain and J. N. Fuchs, Eur. Phys. J. B **83**, 301 (2011).

[35] M. M. Asmar and S. E. Ulloa, Phys. Rev. Lett. **112**, 136602 (2014).

[36] M. Snelder, A. A. Golubov, Y. Asano, and A. Brinkman, J. Phys.: Condens. Matter **27**, 315701 (2015).

[37] G. E. Blonder, M. Tinkham, and T. M. Klapwijk, Phys. Rev. B **25**, 4515 (1982).

[38] C. Bruder, Phys. Rev. B **41**, 4017 (1990).

[39] S. Kashiwaya, Y. Tanaka, M. Koyanagi, and K. Kajimura, Phys. Rev. B **53**, 2667 (1996).

[40] D. Breunig, P. Burset, and B. Trauzettel, Phys. Rev. Lett. **120**, 037701 (2018).

[41] Y. Tanaka and S. Kashiwaya, Phys. Rev. Lett. **74**, 3451 (1995).